

# Gravity currents from a line source in an ambient flow

ANJA C. SLIM<sup>†</sup> AND HERBERT E. HUPPERT

Institute of Theoretical Geophysics, Department of Applied Mathematics and Theoretical Physics,  
Centre for Mathematical Sciences, University of Cambridge, Wilberforce Road,  
Cambridge CB3 0WA, UK

(Received 16 June 2007 and in revised form 11 February 2008)

We present a mainly theoretical study of high-Reynolds-number planar gravity currents in a uniformly flowing deep ambient. The gravity currents are generated by a constant line source of fluid, and may also be supplied with a source of horizontal momentum and a source of particles. We model the motion using a shallow-water approximation and represent the effects of the ambient flow by imposing a Froude-number condition in a moving frame. We present analytic and numerical expressions for the threshold ambient flow speed above which no upstream propagation can occur at long times. For homogeneous gravity currents in an ambient flow below threshold, we find similarity solutions in which the up- and downstream fronts spread at a constant rate and the current propagates indefinitely in both directions. For gravity currents consisting of both interstitial fluid of a different density to the ambient and a sedimenting particle load, we find long-time asymptotic solutions for ambient flow strengths below threshold. These consist of a steady particle-rich near-source region, in which settling and advection of particles balance, and an effectively particle-free frontal region. The homogeneous behaviour of the fronts ensures that they also spread at a constant rate and therefore can propagate upstream indefinitely. For gravity currents driven solely by a sedimenting particle load, we find numerically that a single regime exists for ambient flow strengths below threshold. In these solutions, settling balances advection near the source leading to a steady region, which joins on to a complex frontal boundary layer. The upstream front progressively decelerates. Our solutions for homogeneous and particle-driven gravity currents compare well with published experimental results.

---

## 1. Introduction

In many natural and man-made situations gravity currents are generated by a dense fluid being continually released and spreading horizontally beneath a lighter, flowing ambient. The resulting currents are partly driven by the ambient flow and partly by the buoyancy mismatch: the ambient flow impedes propagation upstream and facilitates propagation downstream. (Note that we reserve the term ‘current’ to refer to the gravity current, and never use it to describe the ambient flow.) Here we study the idealized canonical problem of currents supplied by a constant line source and propagating into a uniform ambient flow at high Reynolds number using a shallow-water formulation. The currents may be homogeneous (uniform

<sup>†</sup> Present address: Department of Mathematics, University of British Columbia, 1984 Mathematics Road, Vancouver, BC, V6T 1Z2, Canada.

density), Boussinesq particle-laden (composed of either dense or light fluid together with a sedimenting particle load) or Boussinesq particle-driven (driven solely by a sedimenting particle load). We investigate how the current evolves and find the threshold value of the ambient flow speed that prevents upstream propagation. For particle-laden and particle-driven currents we also consider the particle deposit distribution.

This problem represents one of the simplest configurations in which an ambient flow affects the dynamics of a gravity current. It is also applicable to a number of natural and environmental phenomena, a particular example being thunderstorm evolution. A frontal rain-band is approximately uniform in the along-front direction and can thus be modelled as two-dimensional (Carbone 1982). Cooling in thunderstorms causes a down-flow that propagates across the ground as a gravity current. It is conjectured that surrounding air forced to rise above the advancing fronts sustains the storm. Often strong winds enhance this vertical motion at the upwind front (Simpson 1997).

Several previous studies have considered continuously supplied Boussinesq homogeneous gravity currents in the presence of an ambient flow, both experimentally (Cederwall 1971; Hogg, Hallworth & Huppert 2005, henceforth referred to as HHH) and using numerical simulations of the full Navier–Stokes equations (Valentine & Kao 1984) or the anelastic equations of motion (Thorpe, Miller & Moncrieff 1980; Liu & Moncrieff 1996). In the inertia–buoyancy regime it was observed that both the upstream and downstream fronts spread at a constant velocity and that the height profiles are approximately uniform far from the source. HHH obtained estimates for the frontal propagation velocities using a box model. In this description both the up- and downstream sections of the current are approximated by a series of rectangles whose areas increase in time at exactly half the volume flux per unit width of the source (an assumption that immediately implies the current propagates upstream into arbitrarily fast ambient flows). All studies except that of HHH reported a maximum ambient flow speed,  $U_c$ , normalized by  $(g'Q)^{1/3}$ , above which upstream propagation does not occur, where  $g'$  is the reduced gravity of the current and  $Q$  is the volume flux per unit width of the source. For particular source configurations, it ranges from approximately  $U_c/(g'Q)^{1/3} = 0.9$  (for the spread of buoyant fluid introduced through a broad slot at the surface of a denser ambient at moderate Reynolds number (Valentine & Kao 1984)) to approximately  $U_c/(g'Q)^{1/3} = 1.4$  (for a current generated by a dense plume descending from a rectangular region of cooling at higher Reynolds number (Thorpe *et al.* 1980; Liu & Moncrieff 1996)). Here we consider these currents using the shallow-water equations, which do not impose a height profile, and we also do not impose the distribution of supplied fluid travelling in each direction. We find similarity solutions that describe the evolution of the current and provide an analytic answer to whether upstream propagation is possible. A key contribution of the present study is the determination of the coefficient as a function of global properties of the source, such as its momentum flux.

The evolution of continuously supplied Boussinesq particle-driven currents in an ambient flow was studied experimentally and numerically using a shallow-water model by HHH. They again assumed that the supplied fluid and particles are distributed equally between the up- and downstream sections of the current. We re-investigate the evolution of these currents, eliminating the assumption of equipartition of the source. We find solutions at later times and a new regime for strong ambient flows. Numerically, it appears that currents in this regime cannot propagate upstream at long times.

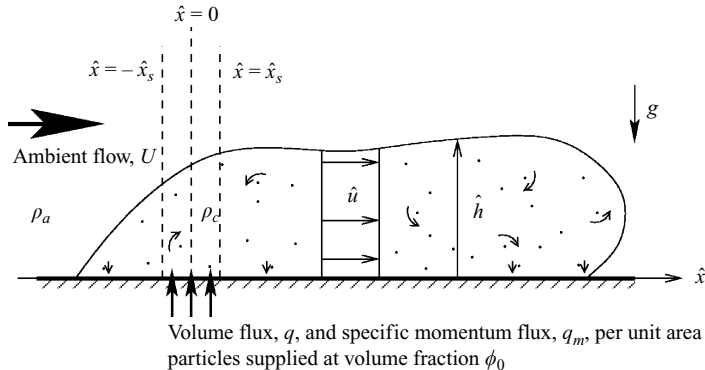


FIGURE 1. A high-Reynolds-number planar gravity current in a uniform ambient flow continuously supplied with fluid, momentum and particles by a source of width  $2\hat{x}_s$ . The system is only constrained by a single horizontal boundary.

To our knowledge, continuously supplied particle-laden currents in an ambient flow have not been considered previously, either experimentally or theoretically. We find long-time asymptotic solutions that describe their evolution and predict whether upstream propagation is possible. The solutions are steady next to the source and are given by homogeneous similarity solutions in moving frames at the fronts.

The outline of this paper is as follows. In §2 we formulate the problem, describing the modifications to the shallow-water model required to capture the ambient flow and the source. In §3 we construct similarity solutions for homogeneous currents, and compare them to the experimental data of HHH. In §4 we address particle-laden and particle-driven currents, constructing long-time asymptotic solutions for particle-laden currents in §4.1. For particle-driven currents we have been unable to find complete asymptotic solutions because of the breakdown of the model at large times. Instead, in §4.2, we present a numerical study of their evolution for varying ambient flow strengths and compare results to the experiments of HHH. In §5 we summarize our major results and briefly discuss the limitations of the model.

## 2. Formulation

We consider a planar gravity current of density  $\rho_c$  propagating into a deep ambient of density  $\rho_a$  over (if it is denser than the ambient) or under (if it is less dense than the ambient) a rigid horizontal boundary. In the ambient there is a far-field uniform flow of velocity  $U > 0$  parallel to the boundary. The current is supplied by a temporally constant source having volume flux,  $q(\hat{x})$ , and specific momentum flux,  $q_m(\hat{x})$ , per unit area, where  $\hat{x}$  is the spatial coordinate. Particles may be homogeneously mixed within the source fluid at volume fraction  $\phi_0$ . This configuration for a current denser than the ambient is shown in figure 1.

### 2.1. Governing equations

Assuming a sufficiently high Reynolds number that viscosity may be ignored, sufficient turbulence that particles and momentum are uniformly distributed in the vertical, neglecting entrainment (for a discussion of its effects see Hallworth *et al.* 1996; Hacker, Linden & Dalziel 1996) and only considering late times when the current is long and thin, we describe the motion in the bulk of a dilute current by the shallow-water equations (e.g. Pedlosky 1987; Bonnetcaze, Huppert & Lister 1993;

Harris, Hogg & Huppert 2001)

$$\frac{\partial \hat{h}}{\partial \hat{t}} + \frac{\partial(\hat{u}\hat{h})}{\partial \hat{x}} = q(\hat{x}), \quad (2.1a)$$

$$\frac{\partial(\hat{u}\hat{h})}{\partial \hat{t}} + \frac{\partial}{\partial \hat{x}} \left( \hat{u}^2 \hat{h} + \frac{1}{2} g' \hat{h}^2 \right) = q_m(\hat{x}), \quad (2.1b)$$

$$\frac{\partial(\hat{\phi}\hat{h})}{\partial \hat{t}} + \frac{\partial(\hat{u}\hat{\phi}\hat{h})}{\partial \hat{x}} = -W_p \hat{\phi} + \phi_0 q(\hat{x}). \quad (2.1c)$$

Here  $\hat{h}$  is the (dimensional) height of the current,  $\hat{u}$  the horizontal velocity,  $\hat{\phi} \ll 1$  the particle volume fraction and  $\hat{t}$  time. The reduced gravity of the system,  $g'$ , is given by  $g' = |\rho_c - \rho_a|g/\rho_c$  for homogeneous currents and  $g' = |\rho_c - \rho_a|g/\rho_a$  for Boussinesq particle-laden and particle-driven currents, where  $\rho_c = [1 - \hat{\phi}(\hat{x}, \hat{t})]\rho_i + \hat{\phi}(\hat{x}, \hat{t})\rho_p$ ,  $\rho_i$  is the density of the interstitial fluid and  $\rho_p$  that of the particles. The unhindered settling velocity of the monodisperse particles is denoted  $W_p$ ; they are not re-entrained.

The functions  $q(\hat{x})$  and  $q_m(\hat{x})$  are non-zero over a finite domain and describe a general source of volume and momentum. For the majority of our investigation we concentrate on the forms

$$q(\hat{x}) = Q/2\hat{x}_s, \quad q_m(\hat{x}) = Q_m/2\hat{x}_s + \text{sgn}(\hat{x})Q_d/\hat{x}_s \quad \text{for } |\hat{x}| \leq \hat{x}_s, \quad (2.2)$$

approximating a simple source in which a volume flux  $Q/2$  is injected with momentum flux  $Q_m/2 - Q_d$  to the left of the origin and a volume flux  $Q/2$  is injected with momentum flux  $Q_m/2 + Q_d$  to the right of the origin. A momentum source is included to reproduce the conditions in the investigation of HHH more accurately. In their experiments, saline or particle-laden water was injected at a constant rate through a small nozzle at the free surface of a tank filled with uniformly flowing fresh water. The resultant downwelling negatively buoyant plume impinged on the base of the tank and spread laterally, rapidly extending to the full width of the tank before propagating up- and downstream as an effectively planar current. Entrainment of ambient fluid during descent of the plume resulted in a net momentum flux (approximated by the term  $Q_m$ ) being supplied to the current, while impingement at the lower boundary transferred vertical momentum from the plume into up- and downstream momentum (approximated by the momentum dipole term  $Q_d$ ). We emphasize that our techniques may be applied to more general source distributions and that for a sufficiently weak dipole the results depend only on the total volume and momentum added (as outlined in Appendix A).

## 2.2. Shock conditions

In our analysis, we shall frequently employ the Rankine–Hugoniot shock conditions and Lax entropy condition, and state them here for future reference (see, for example, Kevorkian 1991) as

$$\llbracket \hat{u}\hat{h} \rrbracket = \hat{S} \llbracket \hat{h} \rrbracket, \quad \llbracket \hat{u}^2 \hat{h} + g' \hat{h}^2 / 2 \rrbracket = \hat{S} \llbracket \hat{u}\hat{h} \rrbracket, \quad (2.3)$$

and

$$\hat{u}_l \pm \hat{c}_l > \hat{S} > \hat{u}_r \pm \hat{c}_r, \quad \hat{u}_l \mp \hat{c}_l < \hat{S} < \hat{u}_r \mp \hat{c}_r, \quad (2.4)$$

respectively. Here  $\llbracket \cdot \rrbracket = (\cdot)_r - (\cdot)_l$  is the difference in the bracketed quantity between the right ( $r$ ) and the left ( $l$ ) across the shock,  $\hat{S}$  is the shock velocity and  $\hat{c} = (g'\hat{h})^{1/2}$  is the celerity. The entropy condition is required to select a unique solution of the shock conditions, demanding that exactly one of the characteristics enters the shock from both sides as time progresses.

### 2.3. Boundary conditions

Closure conditions are required at the upstream and downstream fronts. In addition to describing the resistance of the ambient, they must also describe the influence of the ambient flow (Hallworth, Hogg & Huppert 1998). At the upstream front the intruding current loses momentum as the ambient fluid rises above it. At the downstream front the current may similarly lose momentum, or it may gain momentum if the ambient is flowing faster than the current, inducing a region of low pressure just ahead of it.

For a steadily propagating gravity-current head between ideal Boussinesq fluids

$$\hat{u}_{uf} - U = -\sqrt{2g'\hat{h}_{uf}}, \quad \hat{u}_{df} - U = \sqrt{2g'\hat{h}_{df}}, \quad (2.5)$$

relates the velocity and pressure head at the front (cf. von Kármán 1940; Benjamin 1968). The subscripts  $u$  and  $d$  denote upstream and downstream respectively, and  $f$  the values just behind the front. For ideal fluids this may be used as a closure condition and is consistent with the shallow-water equations (Klemp, Rotunno & Skamarock 1994).

The head of a real gravity current is a complex and unsteady three-dimensional flow and in addition to form drag, there are viscous drag and Reynolds stresses acting upon it. Experimentally (2.5) is found to be modified and may be written as (Simpson & Britter 1980)

$$\hat{u}_{uf} - kU = -\beta\sqrt{g'\hat{h}_{uf}}, \quad \hat{u}_{df} - kU = \beta\sqrt{g'\hat{h}_{df}}, \quad (2.6)$$

where  $k$  is the fraction of the ambient flow velocity felt by the current and  $\beta$  is an imposed frontal Froude number in the frame moving with velocity  $kU$ . Where we explicitly take values for these parameters we set  $\beta=0.91$  and  $k=0.62$ , from the experimental data of Simpson & Britter (1980). (Their experiment investigated currents with height ratios in the range 0.15 to 0.25 relative to the ambient. Similar ratios were also used in the experiments of HHH, and so we take these values for comparison purposes. For deeper ambients  $\beta$  was observed to be closer to  $\sqrt{2}$ .) Explanations for the current experiencing only a fraction of the ambient flow speed are provided by Hallworth *et al.* (1998) and Ross (2000).

The boundary conditions are completed by the kinematic conditions

$$\frac{d\hat{x}_{uf}}{d\hat{t}} = \hat{u}_{uf}, \quad \frac{d\hat{x}_{df}}{d\hat{t}} = \hat{u}_{df}, \quad (2.7)$$

where  $\hat{x}_{uf}$ ,  $\hat{x}_{df}$  are the upstream and downstream front positions respectively. We note that taking values just behind the physical front to impose (2.6) and (2.7) yields numerical and analytical profiles that end much more abruptly than true fronts.

The system (2.1)–(2.7) is also valid for non-Boussinesq homogeneous currents, although  $\beta$  and  $k$  take different values. We discuss solutions for such currents in §3 and thus need to examine how these parameters change. For light currents relative to the ambient,  $\beta$  is small, while for very dense currents it is large (Benjamin 1968; Gröbelbauer, Fanneløp & Britter 1993; Ungarish 2007). To our knowledge, the variation of  $k$  with density contrast has not been explored; however for a low-density current  $k$  might be expected to be close to one, whereas for a high-density current it should be effectively zero. Because  $k$  only enters the governing equations in a product with the parameter  $U$ , its precise value is immaterial to the analysis.

### 2.4. Particle deposit profiles

To complete the description, we give the expression for the particle deposit per unit area,  $\hat{\Phi}(\hat{x}, \hat{t})$ , collected above point  $\hat{x}$  by time  $\hat{t}$ , as

$$\hat{\Phi}(\hat{x}, \hat{t}) = \rho_p W_p \int_0^{\hat{t}} \hat{\phi}(\hat{x}, \hat{t}') d\hat{t}'. \quad (2.8)$$

Finally we note that variations of (2.1)–(2.8) have been extensively and successfully used to study high-Reynolds-number gravity currents in a number of configurations (e.g. Fannelop & Waldman 1972; Houtt 1972; Rottman & Simpson 1983; Bonnecaze *et al.* 1993, 1995). In particular, Hallworth *et al.* (1998) obtained good agreement between similarity solutions, numerical and experimental results for constant-volume homogeneous and particle-driven currents in an ambient flow.

Our numerical code for solving the system (2.1)–(2.8) is described in Appendix B. As initial conditions we set the height and particle volume fraction to be constants and the velocity to be zero inside a small symmetric region neighbouring the source (specific details are given for the solutions presented).

## 3. Homogeneous gravity currents

We begin by considering the evolution of gravity currents driven solely by compositional differences. Such currents are described by the three dimensionless parameters

$$\mathcal{U} = kU/(g'Q)^{1/3}, \quad \mathcal{M} = g'Q_m/(g'Q)^{4/3}, \quad \mathcal{D} = g'Q_d/(g'Q)^{4/3},$$

representing the normalized strength of the ambient flow, normalized net momentum flux and normalized momentum dipole, together with the frontal Froude number,  $\beta$ . For small values of  $\mathcal{U}$ , the source buoyancy flux dominates and we expect the current to be only weakly affected by the ambient flow. Conversely, for large values of  $\mathcal{U}$  it will be strongly affected by the flow and above some threshold value,  $\mathcal{U}_c(\beta, \mathcal{M}, \mathcal{D})$ , it cannot spread upstream at long times. In the next two subsections we present solutions for the height and velocity profiles of the current at long times and find expressions for this threshold value. In §3.3, we compare our solutions with experiments.

### 3.1. Similarity solutions

The system has no intrinsic length scale (assuming that the source scale is no longer relevant) and thus we expect a similarity solution to exist and for profiles to tend towards it. In order to find this global solution, we construct separate similarity solutions in the upstream and downstream sections of the current and join them by conditions across the source.

We commence by presenting the similarity solutions in each section. For a quiescent ambient, Gratton & Vigo (1994) used a phase-plane technique to show that three solution structures are possible, consisting of combinations of sections where  $\hat{u}$  and  $\hat{h}$  are constant and sections where the solution is represented by a rarefaction wave. Using the same approach, it may be readily shown that the same three structures are also the only permissible ones in both the up- and downstream sections of our flowing ambient problem. We classify them below using the nomenclature of Gratton & Vigo (1994) (augmented by the special case type II<sub>s</sub>), and give the expressions for the non-dimensional velocity,  $u = \hat{u}/(g'Q)^{1/3}$ , and celerity,  $c = (g'\hat{h})^{1/2}/(g'Q)^{1/3}$ , in terms of the similarity variable,  $\eta = \hat{x}/(g'Q)^{1/3}\hat{t}$ . The solutions given in (3.1)–(3.3) are written to satisfy the frontal boundary conditions with the

upper sign relating to upstream solutions and the lower to downstream. The Froude numbers at the front and just outside the source are denoted by  $\mathcal{F}_f = u_f/c_f$  and  $\mathcal{F}_s = u_s/c_s$  respectively, with negative values upstream and positive values downstream, on the assumption that flow is outwards from the source region. Using these conventions, we obtain the following four types of similarity solution.

*Type I:* a single constant state given by

$$(u, c) = (\mathcal{F}_f, 1) \frac{1}{\mathcal{F}_f \pm \beta} \mathcal{U}, \quad 0 \leq |\eta| \leq \frac{|\mathcal{F}_f|}{\mathcal{F}_f \pm \beta} \mathcal{U}. \quad (3.1)$$

Such solutions only exist for  $\mathcal{F}_f \geq \mp \beta$ .

*Type II:* two constant states joined by a rarefaction, given by

$$(u, c) = \begin{cases} (\mathcal{F}_s, 1) \frac{1}{\mathcal{F}_s \mp 2} \frac{\mathcal{F}_f \mp 2}{\mathcal{F}_f \pm \beta} \mathcal{U}, & 0 \leq |\eta| \leq |\eta_j|, \\ \frac{1}{3} \left( 2\eta + \frac{\mathcal{F}_f \mp 2}{\mathcal{F}_f \pm \beta} \mathcal{U}, -|\eta| \mp \frac{\mathcal{F}_f \mp 2}{\mathcal{F}_f \pm \beta} \mathcal{U} \right), & |\eta_j| \leq |\eta| \leq \frac{|\mathcal{F}_f \pm 1|}{\mathcal{F}_f \pm \beta} \mathcal{U}, \\ (\mathcal{F}_f, 1) \frac{1}{\mathcal{F}_f \pm \beta} \mathcal{U}, & \frac{|\mathcal{F}_f \pm 1|}{\mathcal{F}_f \pm \beta} \mathcal{U} \leq |\eta| \leq \frac{|\mathcal{F}_f|}{\mathcal{F}_f \pm \beta} \mathcal{U}, \end{cases} \quad (3.2)$$

where  $\eta_j = (\mathcal{F}_s \pm 1)(\mathcal{F}_f \mp 2) \mathcal{U} / (\mathcal{F}_s \mp 2)(\mathcal{F}_f \pm \beta)$  is the value of the similarity variable at the inner join. Such solutions only exist for  $|\mathcal{F}_f| \geq |\mathcal{F}_s| \geq 1$  and  $\mathcal{F}_f \geq \mp \beta$ .

*Type II<sub>s</sub>:* the special form of type II with  $|\mathcal{F}_s| = 1$ , for which  $\eta_j = 0$  and the constant state neighbouring the source is absent.

*Type III:* two constant states joined by a shock, given by

$$(u, c) = \begin{cases} (\mathcal{F}_s, 1) c_s, & 0 \leq |\eta| \leq S, \\ (\mathcal{F}_f, 1) \frac{1}{\mathcal{F}_f \pm \beta} \mathcal{U}, & S \leq |\eta| \leq \frac{|\mathcal{F}_f|}{\mathcal{F}_f \pm \beta} \mathcal{U}, \end{cases} \quad (3.3)$$

where  $S$  is the non-dimensional shock velocity and  $c_s$  the celerity of the near-source solution, both given by the solution of the non-dimensional form of the Rankine–Hugoniot conditions (2.3). Solutions of this type only exist for  $|\mathcal{F}_s| \geq \max(1, |\mathcal{F}_f|)$  and  $\mathcal{F}_f \geq \mp \beta$ , and they are subject to the Lax entropy condition (2.4).

Before proceeding to discuss the required patching between solutions at the source, we briefly describe the physical properties of these different solution types. An example of each is shown in figure 2 (which will be discussed in greater detail below): on the upstream branch all solutions are type I, while progressively further from the source on the downstream branch types II<sub>s</sub>, II and III are observed. The structure selected reflects the ambient resistance to propagation of the current, relative to the strength of the source. If ambient resistance is relatively small, then a current can intrude more readily than it is supplied and at some distance from the source it accelerates and thins (a type II solution). Conversely, if ambient resistance is relatively large, then a current cannot intrude as readily as it is supplied and at some distance from the source it slows and deepens (a type III solution). Finally, if ambient resistance is very large or the source is very weak, then the current is choked and deepening occurs immediately (a type I solution).

We now turn to the description of the source. To specify the complete similarity solution, conditions across it are required in order to select the type of the up- and downstream structures and determine the four unknowns  $\mathcal{F}_{us, ds}$  and  $\mathcal{F}_{uf, df}$ , where subscript *us* (*ds*) indicates values at  $\hat{x} = -\hat{x}_s$  ( $+\hat{x}_s$ ). The form of (2.1) is not conducive

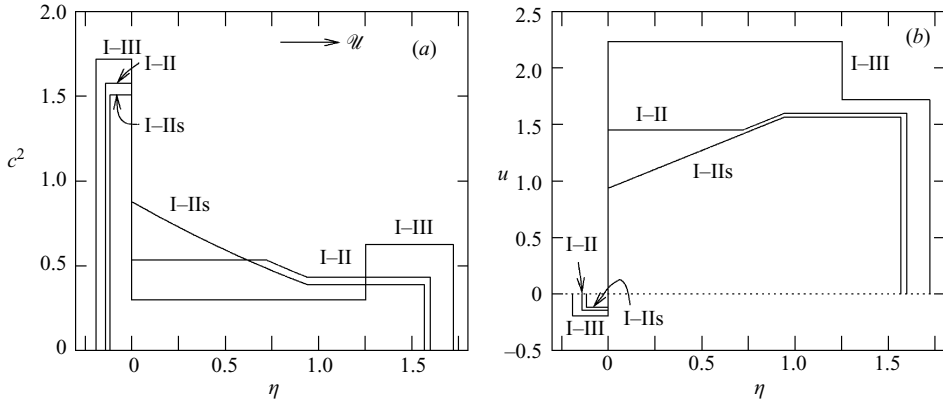


FIGURE 2. (a) Buoyancy and (b) velocity similarity profiles for homogeneous currents with  $\mathcal{U} = 1$ ,  $\mathcal{M} = 0$  and  $\beta = 0.91$ . The profile with smallest up- and downstream extent is for both  $\mathcal{D} = 0$  and  $\mathcal{D} = 0.5$  and is type I–type IIs. The profile of intermediate extent is for  $\mathcal{D} = 1$  and is type I–type II. The profile of greatest extent is for  $\mathcal{D} = 1.5$  and is type I–type III. The location of these solutions in  $(\mathcal{D}, \mathcal{U})$  parameter space is given in figure 3. The notation X–Y denotes a solution that is type X upstream and type Y downstream.

to analysis; a more useful alternative is the following analogy with conditions across a shock. (Gratton & Vigo (1994) did not encounter this complication for a quiescent ambient since they specified the source in terms of its mass flux and its Froude number, rather than its momentum flux.)

(a) The equivalents of the Rankine–Hugoniot conditions are obtained by integrating (2.1) from  $-\hat{x}_s$  to 0 and from 0 to  $\hat{x}_s$ , yielding

$$u_0 c_0^2 - u_{us} c_{us}^2 = 1/2, \quad u_0^2 c_0^2 + c_0^4/2 - u_{us}^2 c_{us}^2 - c_{us}^4/2 = \mathcal{M}/2 - \mathcal{D}, \quad (3.4)$$

$$u_{ds} c_{ds}^2 - u_0 c_0^2 = 1/2, \quad u_{ds}^2 c_{ds}^2 + c_{ds}^4/2 - u_0^2 c_0^2 - c_0^4/2 = \mathcal{M}/2 + \mathcal{D}, \quad (3.5)$$

respectively. These provide four conditions, although also introduce the two new unknowns  $u_0$  and  $c_0$ , denoting the velocity and celerity at  $\hat{x} = 0$ .

(b) The equivalents of the Lax entropy condition provide the final conditions. To specify the states  $u$  and  $c$  on either side of the source, exactly two pieces of information additional to (3.4) and (3.5) must be supplied along characteristics. Thus exactly two characteristics must reach each line  $\hat{x} = \pm \hat{x}_s$ . The possibilities are summarized in table 1, where the plots illustrate the directions of the characteristics  $u \pm c$  just outside the source and at the origin. Further details of this argument are presented in Appendix A, where we discuss conditions for more general source distributions.

Our solutions are now essentially complete: for each possible combination of up- and downstream structures, we now have at most six unknowns ( $\mathcal{F}_{us,ds}$ ,  $\mathcal{F}_{uf,df}$ ,  $c_0$  and  $u_0$ ) and an equal number of conditions ((3.4), (3.5) and table 1), yielding a set of algebraic equations that may be readily solved numerically. For a solution to be valid, it must also satisfy the inequalities outlined in the definitions of types given above and those given in table 1. It appears that these are sufficient to ensure uniqueness of solutions for given parameter values.

Before discussing solution regimes and profiles, we finally note that a substantial simplification is possible for solutions with  $|\mathcal{F}_{us,ds}| \leq 1$  both up- and downstream. In this case  $\mathcal{F}_{us,ds}$  are completely specified by the solution outside the source. Thus (3.4) and (3.5) may be reduced to  $u_{ds} c_{ds}^2 - u_{us} c_{us}^2 = 1$  and  $u_{ds}^2 c_{ds}^2 + c_{ds}^4/2 - u_{us}^2 c_{us}^2 - c_{us}^4/2 = \mathcal{M}$ ,

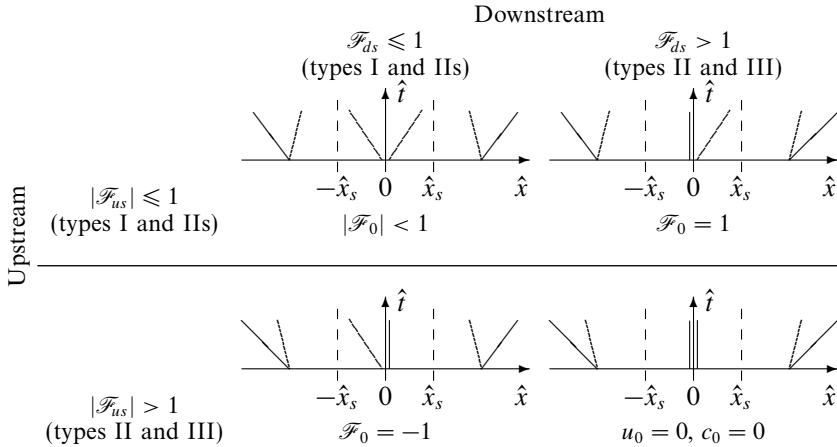


TABLE 1. The possible directions of the characteristics in the vicinity of the source. Here subscript 0 refers to values at the origin. Solutions that are type I and have  $|\mathcal{F}_0| > 1$  on either the up- or downstream section are not included in this classification because they are overdetermined: such solutions only exist on three-dimensional hypersurfaces in our four-dimensional parameter space and we omit them for clarity.

with the full form only required to specify  $u_0$  and  $c_0$ . A consequence is that the momentum dipole only influences the exterior solution once it exceeds a threshold value at which the Froude number at the origin has magnitude unity,  $|\mathcal{F}_0| = 1$ .

### 3.2. Solution regimes

All 16 different combinations for the up- and downstream structures may be shown to be realizable. Regime diagrams illustrating the location of different solution structures in a selection of parameter spaces are given in figure 3: (a) depicts  $(\beta, \mathcal{D})$  space for currents in a quiescent ambient with no net source of momentum, (b) depicts  $(\beta, \mathcal{U})$  space for currents in an ambient flow with no source or dipole of momentum, (c) depicts  $(\mathcal{D}, \mathcal{U})$  space for Boussinesq currents ( $\beta = 0.91$ ) without a net source of momentum, while (d) depicts  $(\mathcal{M}, \mathcal{U})$  space for Boussinesq currents without a dipole of momentum. The behaviour observed is consistent with that anticipated from the qualitative description given earlier: type I solutions are observed for a weak or moderate source (small momentum dipole) and large ambient resistance (light currents in a heavy ambient or, on the upstream side, large ambient flow strengths). Type II solutions are found for a weak source (small momentum dipole or, on the downstream side, an upstream-directed momentum flux) and a weak ambient resistance (heavy currents in a light ambient or, on the downstream side, large ambient flow strengths), while type III solutions are observed for a moderate source and weak ambient resistance. Finally, type III solutions are found whenever the source is very strong. Another important observation is that the presence of a momentum dipole does not alter the solution type until a threshold value is reached in figures 3(a) and 3(c), as predicted in the last paragraph.

The boundary  $\mathcal{U}_c(\beta, \mathcal{M}, \mathcal{D})$ , above which upstream propagation cannot occur at long times, is indicated by solid bold curves in figure 3, and occurs where the upstream frontal velocity is zero. It may be expressed analytically, when both  $2\mathcal{M} \geq 3 - (1 - 1/\beta)^4$

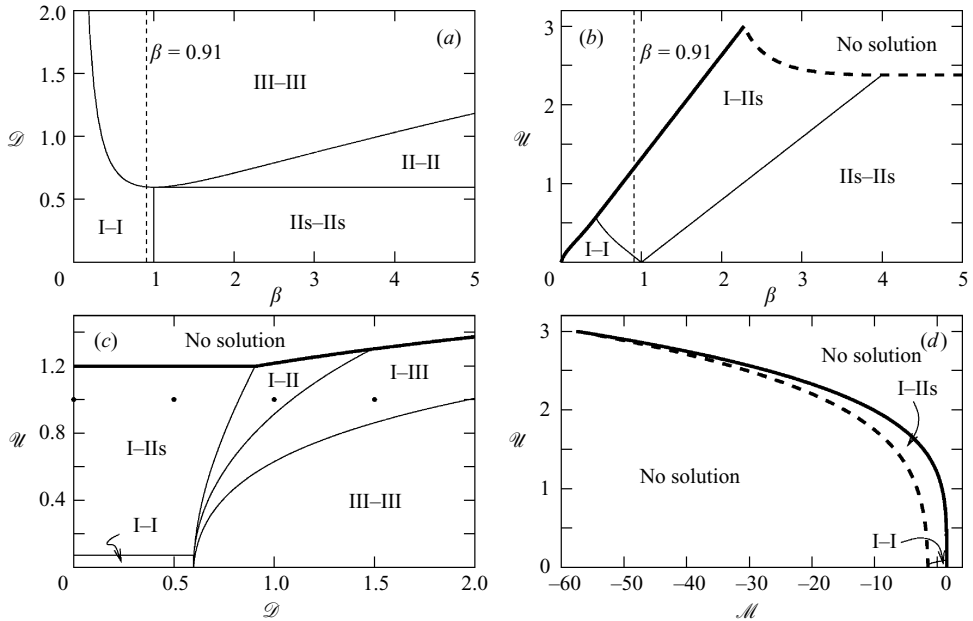


FIGURE 3. Location of the different solution structures in (a)  $(\beta, \mathcal{D})$  parameter space with  $\mathcal{M} = \mathcal{U} = 0$ , (b)  $(\beta, \mathcal{U})$  space with  $\mathcal{M} = \mathcal{D} = 0$ , (c)  $(\mathcal{D}, \mathcal{U})$  space with  $\beta = 0.91$  and  $\mathcal{M} = 0$ , and (d)  $(\mathcal{M}, \mathcal{U})$  space with  $\beta = 0.91$  and  $\mathcal{D} = 0$ . The notation X–Y denotes a solution that is type X upstream and type Y downstream. The dots,  $\bullet$ , in (c) indicate the locations in parameter space of the solution profiles given in figure 2.

and  $\beta \leq 1$  (corresponding to solutions that are not type I downstream), as

$$\mathcal{U}_c = \begin{cases} (3 - 2\mathcal{M})^{1/4} \beta, & \text{for } \mathcal{M} + 2\mathcal{D} + 3/2^{4/3} \leq 3, \\ (3/2^{4/3} + 2\mathcal{D} - \mathcal{M})^{1/4} \beta & \text{otherwise.} \end{cases}$$

The maximum ambient flow speed for which a current can propagate upstream thus depends sensitively on its density relative to the ambient (dense currents, with large  $\beta$ , can propagate into significantly stronger ambient flows than light currents, with small  $\beta$ ) and less sensitively on the net momentum source and the momentum dipole, with the latter only becoming important above a non-zero threshold value.

A second type of boundary beyond which no similarity solutions can be found is indicated by dashed bold curves in figure 3. It occurs where the downstream frontal height becomes zero because of acceleration induced by the faster-flowing ambient. Beyond it, the downstream boundary condition, (2.6b), is no longer valid. The analysis outside this boundary is beyond our scope. However we note that it is of limited physical significance in figure 3(b) since it occurs for dense currents where we expect  $k \ll 1$ . This behaviour is analogous to a dambreak in which the frontal height is zero, which sets its maximum speed of advance (cf. Whitham 1974).

Finally, height and velocity profiles for several regimes are shown in figure 2, with the choice of parameters corresponding to the dots in figure 3(c). A significant observation is that the profiles for the two smallest momentum dipole values are everywhere identical. As the momentum dipole is increased beyond its threshold value, the average speed of the current both up- and downstream increases and the average height decreases correspondingly.

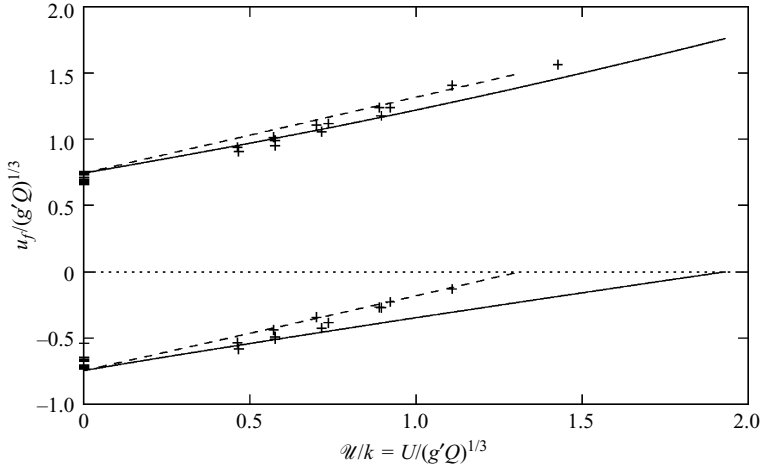


FIGURE 4. The dimensionless velocities of the up- and downstream fronts as functions of the dimensionless ambient flow speed. The symbols are the experimental data of HHH, the solid curve is the similarity solution result with  $\mathcal{M}=0$  and the dashed curve is that with  $\mathcal{M}=0.9 U/k$ ; both have  $\mathcal{D}=0$ .

### 3.3. Comparison with experiments

In order for a comparison between our similarity solutions and experimental data to be valid, the former must be attained within the time frame of the latter. For type I and type II currents numerical and analytic results suggest that the similarity solutions are rapidly achieved, with time scales proportional to the initial volume (Slim 2006, see also Miller & Bernoff 2003).

Figure 4 provides a comparison between model results and the experimental data of HHH. (HHH argued that all their experiments were in the inertia–buoyancy regime. We provide a brief discussion of the time scales for transition to an interfacial drag- or viscous-dominated regime in § 5). In their experimental investigation, HHH observed that the front velocities were effectively constant from initiation; the figure (corresponding to figure 9 of HHH) shows the front velocities of the current, non-dimensionalized by  $(g'Q)^{1/3}$ , as a function of  $U/k = U/(g'Q)^{1/3}$  for both the experiments and our similarity solution with  $\mathcal{D}=0$ . Relatively good agreement is observed, especially when the data are compared to our predictions with  $\mathcal{M}=0.9 U/k$ . With  $\mathcal{M}=0$  the similarity solution and experimental data diverge for  $U/k \gtrsim 0.8$ . A possible explanation for this discrepancy is that interfacial drag becomes important in this range and thus the shallow-water equations are no longer valid: in the limit that the upstream velocity goes to zero, the observed state is a density wedge. However, in the experiments of Simpson & Britter (1980) the current was arrested and presumably interfacial drag was significant, suggesting that some of the effect of drag may already be captured in the imposed value of  $\beta$ . Instead, we propose that entrainment of ambient fluid into the downwelling plume generating the current provides a source of downstream momentum (as also suggested by Cederwall 1971). For the experimental arrangement of HHH,  $\mathcal{M} \approx 0.9 U/k$  (using the model of Hoult, Fay & Forney 1969) and, as observed above, agreement is indeed improved for larger  $U$  by adding its effect.

Despite the good agreement in the frontal velocities between theory and experiments, the profiles of the shallow-water solutions and the experiments agree less

well: for the shallow-water results the upstream section is thicker than the downstream (this has also been found in numerical simulations by Valentine & Kao 1984 and Liu & Moncrieff 1996), whereas the reverse can be inferred from the experiments of Hallworth *et al.* (1998) and HHH. The disagreement may result from motion in the ambient (Hallworth *et al.* 1998), neglected in our infinite-ambient model, since the experimental currents filled about a third of the depth of the tank. The fact that good agreement for the front velocities is nevertheless observed might suggest that the essential physics is captured by the frontal Froude number and the source conditions; the precise dynamics within the bulk of the current and ambient is of secondary importance. An alternative explanation is that entrainment preferentially deepens the thin downstream section of the current without altering its buoyancy (although concomitant entrainment of momentum presumably modifies the solution structure more subtly); and therefore a comparison between experimental and theoretical buoyancy profiles would be more correct. Unfortunately, to our knowledge, such measurements are not available for this configuration.

In summary, we have presented a framework for finding similarity solutions for a homogeneous gravity current in a uniform ambient flow with a source specified by its mass and momentum fluxes. A total of 16 different regimes are feasible depending on the momentum supplied to the current, the ambient resistance and the ambient flow speed. For sufficiently strong ambient flow speeds a solution with an upstream section does not exist at long times (and any initial upstream propagation is dependent on the initial condition). Our frontal velocities compare well with experiments.

#### 4. Particle-laden and particle-driven gravity currents

Gravity currents in which particles contribute to the driving density difference are more complex than their homogeneous counterparts because the buoyancy force changes continuously as particles are advected and settle out of suspension. Similarity solutions are no longer possible because a length scale exists: the typical distance over which particles are advected as they settle,  $Q/W_p$ . Nevertheless some long-time asymptotic solutions may still be found as we describe below (see also Harris *et al.* 2001, for alternative techniques).

Using unhatted symbols to denote non-dimensional and rescaled variables, we non-dimensionalize and rescale the governing equations based on the length scale of settling and the velocity scale of the particle source by

$$\left. \begin{aligned} \hat{x} &= (Q/W_p)x, & \hat{t} &= [Q/W_p(g'_p\phi_0 Q)^{1/3}]t, \\ \hat{h} &= [Q/(g'_p\phi_0 Q)^{1/3}]h, & \hat{u} &= (g'_p\phi_0 Q)^{1/3}u, & \hat{\phi} &= \phi_0\phi, \end{aligned} \right\} \quad (4.1)$$

where  $g'_p = (\rho_p - \rho_i)g/\rho_a$ . Substituting (4.1) into (2.1) we obtain

$$\frac{\partial \hat{h}}{\partial \hat{t}} + \frac{\partial(\hat{u}\hat{h})}{\partial \hat{x}} = \frac{1}{2x_s} \Theta(x_s - |\hat{x}|), \quad (4.2a)$$

$$\frac{\partial(\hat{u}\hat{h})}{\partial \hat{t}} + \frac{\partial}{\partial \hat{x}} \left[ \hat{u}^2 \hat{h} + \frac{1}{2} |\gamma + \phi| \hat{h}^2 \right] = 0, \quad (4.2b)$$

$$\frac{\partial(\hat{\phi}\hat{h})}{\partial \hat{t}} + \frac{\partial(\hat{u}\hat{\phi}\hat{h})}{\partial \hat{x}} = -\hat{\phi} + \frac{1}{2x_s} \Theta(x_s - |\hat{x}|), \quad (4.2c)$$

where we ignore any source of momentum for simplicity,  $\Theta(\cdot)$  is the Heaviside function and  $x_s = W_p \hat{x}_s / Q$ . Here

$$\gamma = \frac{g'_i}{g'_p \phi_0}$$

is the ratio of the buoyancy source due to interstitial fluid to that due to particles, and  $g'_i = (\rho_i - \rho_a)g / \rho_a$ . Dense currents propagating over a lower boundary have  $\gamma + \phi > 0$ , while light currents propagating below an upper boundary have  $\gamma + \phi < 0$ . Values of  $\gamma$  large (small) in magnitude indicate that the buoyancy flux is dominated by the addition of interstitial fluid (particles). The limit  $\gamma \rightarrow 0$  corresponds to a purely particle-driven current.

The frontal boundary conditions (2.6) and (2.7) become

$$\frac{dx_{uf}}{dt} = u_{uf}, \quad u_{uf} - \mathcal{U}_p = -\beta \sqrt{|\gamma + \phi_{uf}| h_{uf}}, \quad (4.3)$$

$$\frac{dx_{df}}{dt} = u_{df}, \quad u_{df} - \mathcal{U}_p = \beta \sqrt{|\gamma + \phi_{df}| h_{df}}, \quad (4.4)$$

where

$$\mathcal{U}_p = kU / (g'_p \phi_0 Q)^{1/3}.$$

The deposit, non-dimensionalized by  $\rho_p(\phi_0^2 Q^2 / g'_p)^{1/3}$ , is  $\Phi(x, t) = \int_0^t \phi(x, t') dt'$ .

#### 4.1. Particle-laden gravity currents

We begin by considering numerical solutions for particle-laden currents. Sample height, velocity, particle volume fraction and (scaled) deposit profiles at different times are shown for  $\mathcal{U}_p = 1.2$ ,  $\gamma = 1$  and  $\beta = 0.91$  in figure 5. At early times, the height and velocity profiles are reminiscent of the homogeneous similarity solution with the equivalent density difference (as suggested by the fair agreement between the numerical solution and the corresponding homogeneous similarity solution at  $t = 1$  in figure 5c). This balance is progressively eroded, on a time scale of order unity, as particles settle. Nearest the source, particles are completely replenished, but further away depleted fluid cannot completely replenish the current ahead of it. At long times, a new balance develops close to the source between particle advection and settling. In this region the solution is steady, the particle volume fraction decays exponentially away from the source (figure 5d) and the height and velocity tend to constant values (figures 5a and 5b). At the fronts, the current is effectively devoid of particles and the length scale associated with settling is no longer relevant there. The current appears homogeneous, with homogeneous similarity solutions observed in a moving frame.

##### 4.1.1. Long-time asymptotic solutions

Using the numerical results for guidance, we look for asymptotic solutions consisting of steady near-source solutions (which we refer to as the *interior* solutions, although exterior to the source proper) and homogeneous solutions at the fronts (which we refer to as the *frontal* solutions).

Interior solutions of (4.2) satisfy

$$u_{ui} h_{ui} = \mathcal{A}, \quad u_{ui}^2 h_{ui} + \frac{1}{2} |\gamma + \phi_{ui}| h_{ui}^2 = \mathcal{B}, \quad \phi = e^{-x/\mathcal{L}} \quad (x < -x_s), \quad (4.5a-c)$$

$$u_{di} h_{di} = 1 + \mathcal{A}, \quad u_{di}^2 h_{di} + \frac{1}{2} |\gamma + \phi_{di}| h_{di}^2 = \mathcal{B}, \quad \phi = e^{-x/(1+\mathcal{L})} \quad (x > x_s), \quad (4.6a-c)$$

where subscript  $i$  denotes interior;  $\mathcal{A} \leq 0$  and  $\mathcal{B}$  are constants of integration and we have assumed  $x_s \ll 1$ . For large  $x$  in this near-source solution,  $\phi \rightarrow 0$  and  $h$  and

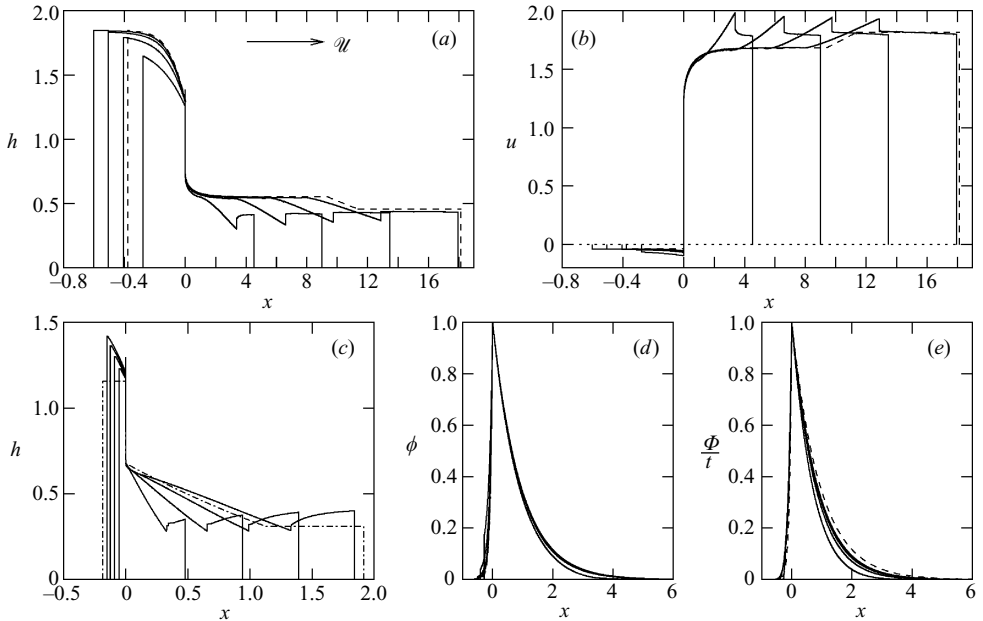


FIGURE 5. Numerical (a) height, (b) velocity, (d) particle volume fraction and (e) scaled deposit profiles at times  $t = 2.5, 5, 7.5$  and  $10$  for a particle-laden gravity current with  $\mathcal{U}_p = 1.2$ ,  $\gamma = 1$  and  $\beta = 0.91$ . The dashed curve is the asymptotic solution at  $t = 10$ . The height at early times ( $t = 0.25, 0.5, 0.75$  and  $1$ ) is shown in (c) where the dash-dotted curve is the homogeneous similarity solution at  $t = 1$ . Note the expanded  $x$ -axis for  $x < 0$  in (a) and (b). The initial conditions are  $h = \phi = 1$  and  $u = 0$  for  $|x| \leq 0.01$ . The source occupies  $|x| \leq 0.0005$ .

$u$  tend to constant values. We note that at a given  $x$ , both  $h$  and  $u$  are solutions to cubic equations; uniqueness is ensured by the condition that the source cannot be supercritical in the absence of a source of momentum. We justify this in Appendix A.

Matching (4.5a–c) and (4.6a–c) to a solution satisfying the appropriate frontal boundary condition can be done in two ways. The most obvious is that the constant far-field interior solution itself satisfies (4.3) or (4.4) (the upstream section of figure 5). A second way is to connect it to a homogeneous similarity solution in a moving frame (the downstream section of figure 5). This connection can be either via a shock or continuous.

If the connection is via a shock, then the Rankine–Hugoniot conditions (2.3) apply across it and the frame moves at the non-dimensional shock velocity,  $S$ . Requiring that flow is away from the source in both the stationary frame and the frame of the shock, we find that  $|\mathcal{F}_{uf,df}^s| < 1$  and

$$|\mathcal{F}_{ui\infty,di\infty}| > 1 \quad (4.7a)$$

from the Lax entropy condition (2.4), where the superscript  $s$  indicates the Froude number in the frame of the shock and the subscript  $i\infty$  indicates the far-field interior solution. The former condition implies that the frontal homogeneous similarity solution is type I (i.e. constant).

If the connection is continuous, then the frame moves at the velocity of one of the characteristics of the (constant) far-field interior solution (Lax 1957). Thus a join on the up- or downstream section travels at a velocity  $u_{ui\infty} + c_{ui\infty}$  or  $u_{di\infty} - c_{di\infty}$  respectively (requiring flow outward from the source in the moving frame imposes

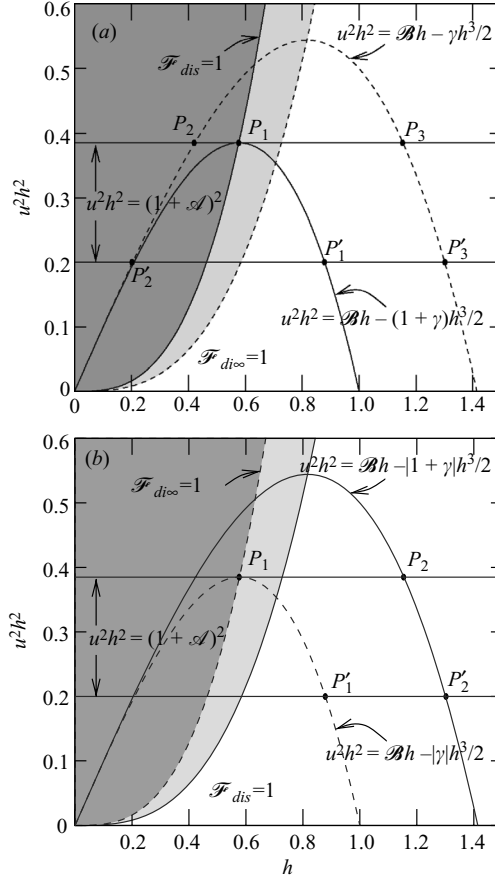


FIGURE 6. The  $(h, u^2 h^2)$  space for the downstream section of the interior solution for (a)  $\gamma > 0$  and (b)  $\gamma < -1$ . The solid curves apply at the source ( $x = x_s$ ) where  $\phi = 1$ . The dashed curves apply in the far field ( $x \gg 1$ ) where  $\phi = 0$ . Points in both the lighter and darker shaded regions have  $|\mathcal{F}_{dis\infty}| > 1$ ; points in the darker shaded region also have  $|\mathcal{F}_{dis}| > 1$ . The curves selected to represent  $u^2 h^2 = (1 + \mathcal{A})^2$  apply both in the near and far fields.

the choice of characteristic). Because the join must move outwards from the source, the Froude number in the far field satisfies

$$|\mathcal{F}_{ui\infty, di\infty}| \geq 1. \quad (4.7b)$$

The magnitude of the Froude number in the moving frame is unity. Thus the connecting similarity solution must be type IIs.

Having described the structure and conditions for the different types of connection, we proceed to find the possible solution regimes by employing a graphical argument and commence with the case  $\gamma > 0$ . Equations (4.5) and (4.6) may be represented by curves in  $(h, u^2 h^2)$  space whose intersections yield possible solution states  $u$  and  $h$  for a given  $x$ . Figure 6(a) shows the  $(h, u^2 h^2)$  space for the downstream section of the interior solution with  $\gamma > 0$ . Two horizontal lines are drawn for which the  $(h, u^2 h^2)$  pairs satisfy the mass flux condition (4.6) for two different values of the (as yet unknown) constant  $\mathcal{A}$ . On the curves  $u^2 h^2 = \mathcal{B}h - (1 + \gamma)h^3/2$  and  $u^2 h^2 = \mathcal{B}h - \gamma h^3/2$ , the  $(h, u^2 h^2)$  pairs satisfy the momentum flux condition (4.6 b), for some value of the constant  $\mathcal{B}$ , at the source ( $x = x_s$ ) and in the far field ( $x \gg 1$ ) respectively. Intersection

points of the two families of curves give possible interior states (for example points  $P_1$  or  $P'_1$  at the source and points  $P_2$ ,  $P'_2$ ,  $P_3$  or  $P'_3$  in the far field).

On the curves  $|\mathcal{F}_{dis}| = 1$  and  $|\mathcal{F}_{di\infty}| = 1$ , the  $(h, u^2h^2)$  pairs have a Froude number of magnitude unity at the source and in the far field respectively. These curves pass through the local maxima of the corresponding momentum flux curves. To the left of each curve  $|\mathcal{F}_{di}| > 1$  and to the right  $|\mathcal{F}_{di}| < 1$ . We require  $|\mathcal{F}_{dis}| \leq 1$  in the absence of a momentum dipole. If  $|\mathcal{F}_{dis}| < 1$ , then the solution at the source is represented by a point such as  $P'_1$  in figure 6(a). Continuity in  $x$  (a steady shock cannot satisfy the Lax entropy condition) demands that the far-field solution also has  $|\mathcal{F}_{dis}| < 1$ , and is represented by the point  $P'_3$ . Because this solution has  $|\mathcal{F}_{di\infty}| < 1$ , it must also be the frontal state since the other forms of connection are precluded by (4.7). Conversely, if  $|\mathcal{F}_{dis}| = 1$ , then the solution at the source is represented by the point  $P_1$  and in the interior far from the source by the point  $P_2$  (the point  $P_3$  would be overdetermined). The point  $P_2$  has  $|\mathcal{F}_{di\infty}| > 1$  and so may connect to the frontal state via a shock or by a continuous connection to a homogeneous similarity solution.

In summary, for  $\gamma > 0$  the up- and downstream solutions can both take one of the following three forms.

*Type I:* the interior solution has  $|\mathcal{F}_{is}| < 1$  and satisfies the frontal boundary condition directly.

*Type III:* the interior solution has  $|\mathcal{F}_{is}| = 1$  and connects via a shock to a constant frontal state.

*Type IIIi:* the interior solution has  $|\mathcal{F}_{is}| = 1$  and connects continuously to a homogeneous similarity solution in a moving frame.

For  $\gamma < -1$ , performing a similar graphical argument on figure 6(b), we find the following forms of solution.

*Type II:* the interior solution has  $|\mathcal{F}_{is}| < |\mathcal{F}_{i\infty}| < 1$  and satisfies the frontal boundary condition directly. We label it distinctly from the equivalent type for  $\gamma > 0$  because it is structurally different, with the height decreasing away from the source rather than increasing.

*Type IIIi:* the interior solution has  $|\mathcal{F}_{is}| < 1$  and  $|\mathcal{F}_{i\infty}| = 1$  and connects continuously to a homogeneous similarity solution in a moving frame.

Solutions to the algebraic equations (4.3)–(4.6), together with (2.3) or (3.2) for a type-IIIi or types-IIIi and IIIii solution respectively, now fully specify the asymptotic solutions of the governing equations.

#### 4.1.2. Solutions and parameter spaces

The location of solution regimes in  $(\beta, \mathcal{U}_p)$  parameter space for  $\gamma = 1$  is shown in figure 7(a). It is similar to that for homogeneous currents, figure 3(b), with additional sub-regimes and solutions existing for stronger ambient flows because the source of particles provides an additional buoyancy force. We emphasize that the governing equations are not strictly valid for non-Boussinesq particle-laden currents, and so only the range  $0.7 \lesssim \beta \lesssim \sqrt{2}$  of the figure is physically relevant. We include a broader range of  $\beta$  to illustrate the different asymptotic structures. The change in solution structure with changing balance between particles and interstitial fluid in the driving density difference is illustrated by the  $(1/\gamma, |\gamma|^{-1/3}\mathcal{U}_p)$  parameter space for  $\beta = 0.91$  shown in figure 7(b). Solutions that are type II both up- and downstream occur when the ambient flow is weak and the current is driven mainly by particles. Solutions that are type I or II both up- and downstream occur for very weak ambient flows and light currents or almost homogeneous dense currents. Type I upstream and type II

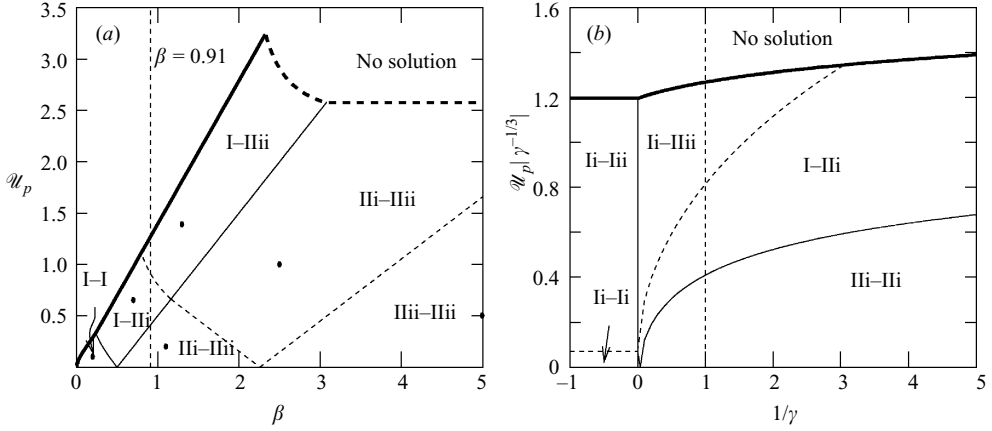


FIGURE 7. The location of solution regimes in (a)  $(\beta, \mathcal{U}_p)$  parameter space with  $\gamma = 1$  and (b)  $(1/\gamma, |\gamma|^{-1/3}\mathcal{U}_p)$  parameter space with  $\beta = 0.91$ . The notation X–Y refers to a type-X solution upstream and a type-Y solution downstream. The dots,  $\bullet$ , indicate the parameter space locations of the profiles in figure 8.

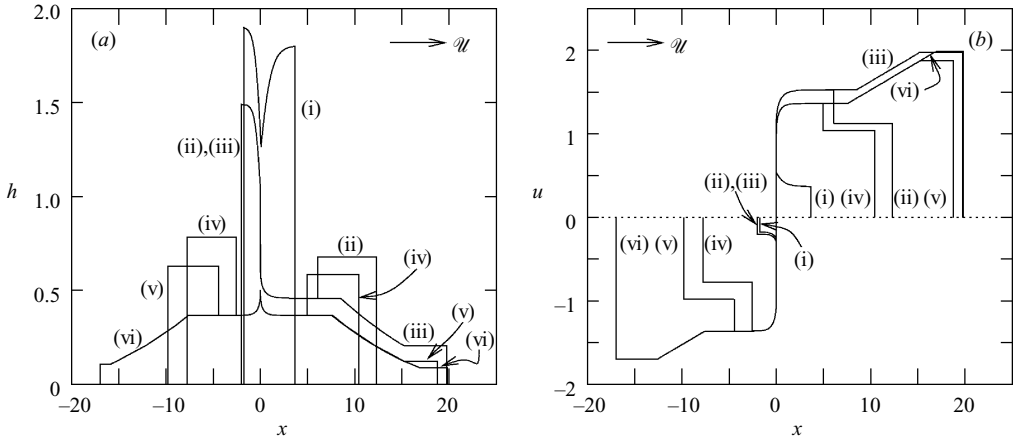


FIGURE 8. (a) Height and (b) velocity profiles, at non-dimensional time equal to 10, for particle-laden gravity currents in six possible regimes. The parameter values are  $\gamma = 1$  and (i)  $\beta = 0.2$ ,  $\mathcal{U}_p = 0.1$  (I–I); (ii)  $\beta = 0.7$ ,  $\mathcal{U}_p = 0.65$  (I–II); (iii)  $\beta = 1.3$ ,  $\mathcal{U}_p = 1.39$  (I–III); (iv)  $\beta = 1.1$ ,  $\mathcal{U}_p = 0.2$  (II–II); (v)  $\beta = 2.5$ ,  $\mathcal{U}_p = 1$  (II–III); and (vi)  $\beta = 5$ ,  $\mathcal{U}_p = 0.5$  (II–III). The notation X–Y indicates a type-X solution upstream and a type-Y solution downstream.

downstream currents (respectively, type Ii and Iii for light currents) occur for strong ambient flows.

As with homogeneous currents, there are two families of boundaries beyond which asymptotic solutions of the assumed form do not exist. The solid bold curves in figure 7 indicate where the upstream frontal velocity is zero; above them no solutions with an upstream propagating section exist. For solutions that are not type I or Ii downstream, these curves are given by  $\mathcal{U}_{pc} = 3^{1/4}|\gamma|^{1/3}[1 + \max(0, 1/\gamma)]^{1/12}\beta$ . The dashed bold curve in figure 7(a) indicates where the downstream height becomes zero.

Typical height and velocity profiles for each regime are shown in figure 8. Where solutions are type I, the ambient strongly resists the advance of the current, slowing and deepening it away from the source. Where solutions are type II, the ambient

resistance is weaker and the current can intrude more readily than it is supplied. The flow accelerates and thins away from the source, becoming supercritical. Hence information about the precise nature of the frontal resistance cannot reach the source. In type-IIi solutions, the far-field flow produced by the source is too strong: the current cannot intrude into the ambient as readily as it is supplied. The flow is slowed and deepened again by a shock. In type-IIii solutions, the far-field flow is too weak: the current can intrude more readily than it is supplied from the interior and it accelerates and thins further, through a rarefaction.

We conclude this subsection by noting that figure 5 shows fairly good agreement between the numerical and the long-time asymptotic solutions at  $t = 10$ .

#### 4.1.3. Particle deposit profiles

The deposit at long times may easily be calculated using (4.5c) and (4.6c) to be

$$\Phi = \begin{cases} t e^{-x/\mathcal{A}} & \text{for } x < 0, \\ t e^{-x/(1+\mathcal{A})} & \text{for } x > 0. \end{cases}$$

For solutions that are type II both up- and downstream, the deposit is symmetric. Otherwise, at a given distance from the source, it is deeper downstream than upstream.

### 4.2. Particle-driven gravity currents

We now turn our attention to currents driven solely by a sedimenting particle load. For this case, HHH found numerical solutions of (4.2)–(4.4) under the assumption that the supplied fluid and particles are equally distributed up- and downstream. They obtained good agreement between their numerical and experimental frontal velocities. We consider these flows in more detail, exploring the structure of solutions and eliminating the assumption of equal partition of the source. As in §4.1, there is no similarity solution because a (dimensional) length scale,  $Q/W_p$ , exists. Unlike in §4.1, we have been unable to find a complete asymptotic solution at long times and instead we discuss numerical results that highlight typical properties.

For  $\beta = 0.91$ , a study of parameter space suggests that at long times there are two possible regimes: one in which the ambient flow is weak ( $\mathcal{U}_p < \mathcal{U}_{pc} \approx 0.37$ ) and the source is equally partitioned; and one in which the ambient flow is strong ( $\mathcal{U}_{pc} < \mathcal{U}_p < \mathcal{U}_c(0.91) \approx 1.20$ ) and the source fluxes are unequal. The evolution of the height, velocity, particle volume fraction and deposit profiles for currents in the two regimes is shown in figures 9 and 10 for representative values  $\mathcal{U}_p = 0.1$  and  $\mathcal{U}_p = 0.8$  respectively.

In both regimes, the solution initially tends towards the homogeneous similarity solution having  $\mathcal{U} = \mathcal{U}_p$  (suggested in the insets in figures 9a and 10a; cf. particle-laden gravity currents in §4.1). However, this balance is progressively eroded as particles settle.

For a weak ambient flow, the pressure gradient induced by the decaying particle profile causes the current to accelerate and thin away from the source until it catches the slower moving front and abruptly deepens (figures 9a and 9b). Neighbouring the source, a symmetric steady solution develops that is unaffected by the ambient flow. It is given implicitly by

$$\left. \begin{aligned} uh = -\mathcal{A}, \quad u^2h + \frac{1}{2}\phi h^2 = \mathcal{B}, \quad \phi = e^{-x/\mathcal{A}} & \quad \text{for } x < 0, \\ uh = 1 + \mathcal{A}, \quad u^2h + \frac{1}{2}\phi h^2 = \mathcal{B}, \quad \phi = e^{-x/(1+\mathcal{A})} & \quad \text{for } x > 0, \end{aligned} \right\} \quad (4.8)$$

with  $\mathcal{A} = -1/2$  and  $\mathcal{B} = 3/4$ , and is equivalent to the interior solutions of type II–type II particle-laden currents (cf. profiles (iv)–(vi) in figure 8). This solution connects to

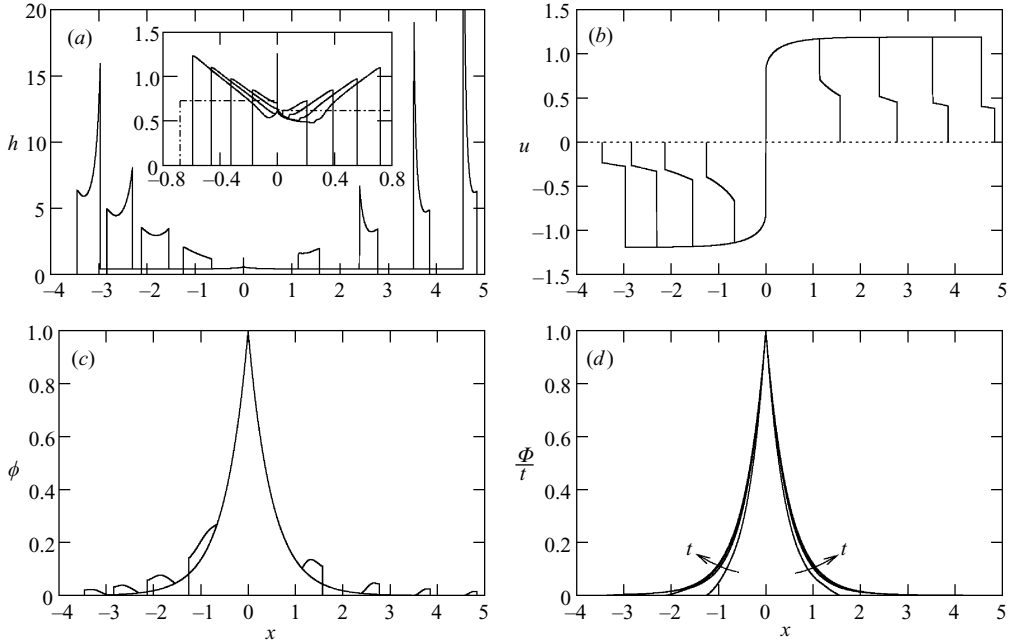


FIGURE 9. (a) Height, (b) velocity, (c) particle volume fraction and (d) scaled deposit profiles at times  $t = 2.5, 5, 7.5$  and  $10$  for  $\mathcal{U}_p = 0.1$  and  $\beta = 0.91$ . The inset in (a) shows height profiles at times  $t = 0.25, 0.5, 0.75$  and  $1$ , where the dash-dotted curve is the homogeneous similarity profile at  $t = 1$  in the absence of particle settling (it extends marginally beyond the scales of the plot). Note that the downstream shock at  $t = 10$  has  $h > 20$  and is cut off in (a). The ambient flow is from left to right. The initial conditions are  $h = \phi = 1$  and  $u = 0$  for  $|x| \leq 0.01$ . The source occupies  $|x| \leq 0.0005$ .

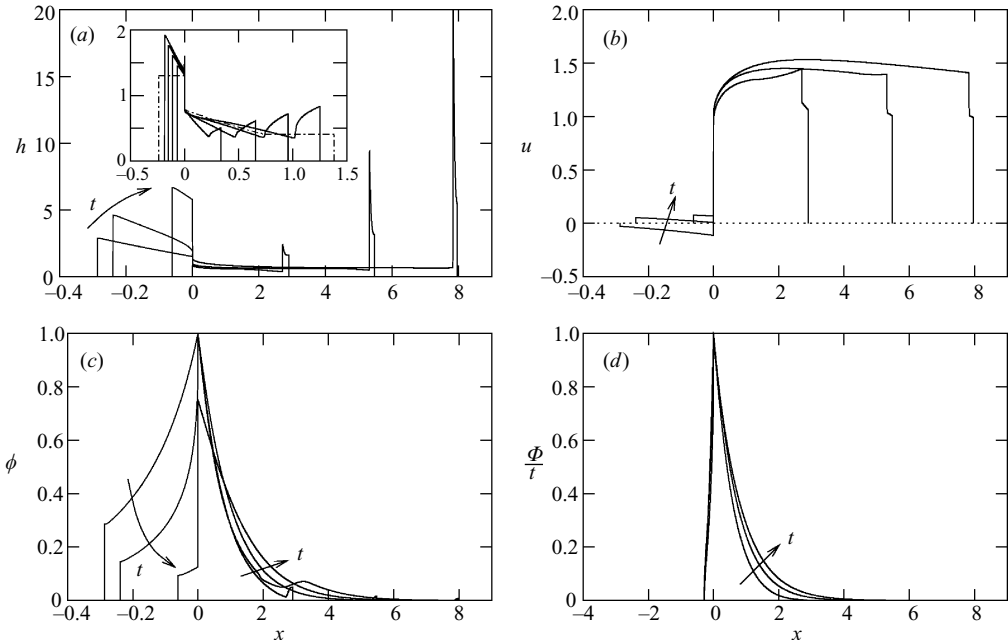


FIGURE 10. As figure 9 but with  $\mathcal{U}_p = 0.8$  for  $t = 2.5, 5$  and  $7.5$ . Note the expanded  $x$ -axis for  $x < 0$  in (a–c), but not for (d). The downstream shock at  $t = 7.5$  has  $h > 20$  and is cut off in (a).

a deep, relatively particle-rich frontal boundary layer. Such an evolution is similar to that observed theoretically for constantly supplied axisymmetric particle-driven currents in a quiescent ambient (Bonnetcaze *et al.* 1995).

For a strong ambient flow the downstream evolution away from the homogeneous solution is similar. However the ambient flow provides greater resistance to the upstream propagation of the current and prevents the upstream section accelerating and thinning in the same manner. Instead the current deepens away from the source. This regime is analogous to type I–type II particle-laden currents, although the interior solution is not steady since (4.8) (with unknown constants  $\mathcal{A}$  and  $\mathcal{B}$ ) cannot satisfy the frontal boundary condition (4.3). Instead, the solution evolves, and in figure 10 the upstream front is retreating at  $t = 5$  and  $7.5$  (figure 10*b*).

At long times a large shock joins the frontal boundary layer to the interior in both regimes, which is unlikely to be physically meaningful. The laminar model of Ungarish & Huppert (1998) may be more appropriate at such times, but this extension is beyond our scope.

For the weak flow regime we could not determine under what conditions the initially upstream-propagating front eventually retreats. For flow strengths close to  $\mathcal{U}_{pc} \approx 0.37$  it always does so. For very weak flows, we found retreat at very long times in some calculations. This was always outside the domain of validity of the shallow-water equations, and may have been due to insufficient resolution of the shock. For the strong flow regime, the upstream front always appears to retreat. The reason such a current can propagate upstream at all is because it initially behaves as a homogeneous current.

The evolution of the deposit is shown in figures 9(*d*) and 10(*d*) for weak and strong ambient flows respectively. For weak flows, the deposit is symmetric about the source and to leading order is proportional to  $t \exp(-2|x|)$  at long times, as was also observed by HHH. For strong flows it is deeper downstream than upstream.

A comparison between our numerical results and the experimental data of HHH is shown in figure 11 (corresponding to their figure 16), indicating reasonable agreement. As discussed in §3, for stronger ambient flows the net source of momentum may be significant and including it may improve agreement (particularly in figure 11*d*). We note that our results do not show any better agreement with the data than the results of HHH, despite three of the four experimental ambient flow strengths being in the strong flow regime (so an assumption of equal partition of the source is not appropriate). A possible explanation for this coincidence is that HHH took  $k = 1$ , thus effectively increasing the ambient flow strength. This in some sense counteracts the increased (decreased) tendency to spread upstream (downstream) due to increased (decreased) supply of fluid upstream (downstream).

## 5. Conclusions

We have presented a series of solutions to describe constantly supplied homogeneous particle-laden and particle-driven gravity currents in a uniform ambient flow. The behaviour of currents is determined by the normalized strength of the ambient flow and the normalized momentum source and dipole. For particle-laden currents the ratio of the buoyancy flux due to the interstitial fluid to that due to particles,  $\gamma$  (negative for light currents and positive for dense currents), is also important.

For homogeneous currents, we found 16 possible forms of similarity solution describing the intermediate asymptotics. A unique form is selected for given source

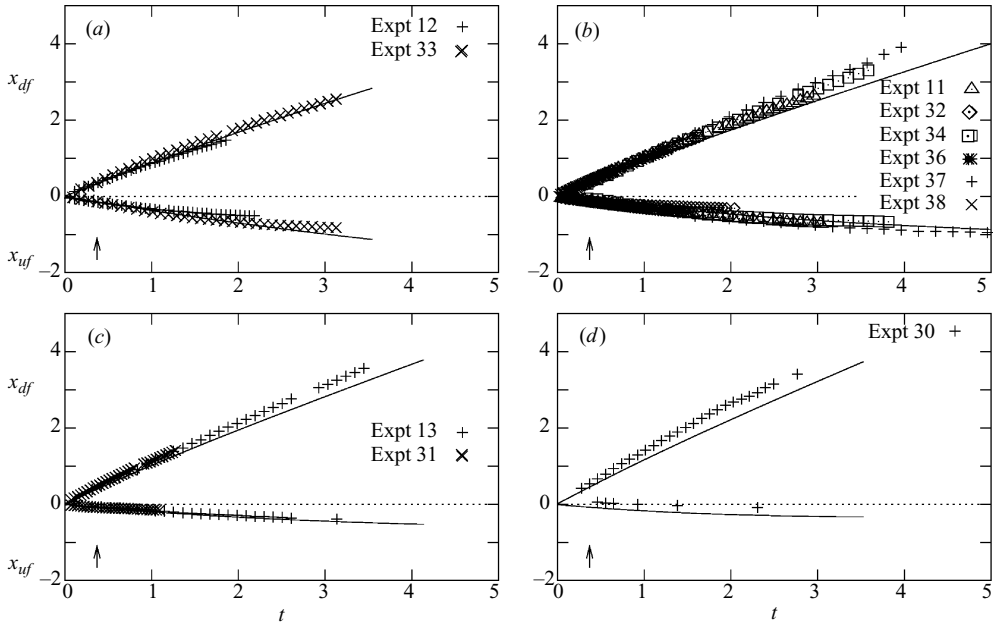


FIGURE 11. Upstream and downstream front positions against time for the experimental particle-driven currents of HHH (symbols) and for the corresponding numerical solutions assuming no source of momentum (curves). For the numerical solutions we take (a)  $\mathcal{U}_p/k = 0.57$ , (b)  $\mathcal{U}_p/k = 0.73$ , (c)  $\mathcal{U}_p/k = 0.91$  and (d)  $\mathcal{U}_p/k = 1.15$ .

and frontal parameters. Any change in the ambient flow velocity or the net momentum flux alters the observed solution, whereas a momentum dipole only affects the solution above a threshold value. We have also presented an analytical prediction for the ambient flow speed above which a current cannot penetrate arbitrarily far upstream, given by

$$\mathcal{U}_c = \begin{cases} (3 - 2\mathcal{M})^{1/4}\beta, & \text{for } \mathcal{M} + 2\mathcal{D} + 3/2^{4/3} \leq 3, \\ (3/2^{4/3} + 2\mathcal{D} - \mathcal{M})^{1/4}\beta & \text{otherwise,} \end{cases}$$

when both  $2\mathcal{M} \geq 3 - (1 - 1/\beta)^4$  and  $\beta \leq 1$  (corresponding to solutions that are not type I downstream) with the dipole dependence specific to the simple source given by (2.2).

For particle-laden currents in the absence of any source of momentum, we found six families of long-time asymptotic solutions. These consist of steady solutions close to the source, in which the particle volume fraction decays exponentially, which connect to homogeneous similarity solutions in moving frames at the fronts. For  $\mathcal{U} > 3^{1/4}|\gamma|^{1/3}[1 + \max(0, 1/\gamma)]^{1/12}\beta$  the current cannot penetrate arbitrarily far upstream at long times (in the absence of any source of momentum, and where the downstream solution is not type I or Ii).

We note that supplied fluid and particles are equally distributed up- and downstream only for dense non-Boussinesq homogeneous currents and particle-dominated particle-laden currents in weak ambient flows. For other types of current and stronger ambient flows, the downstream section is always more voluminous.

For particle-driven currents, we conducted a numerical study for  $\beta = 0.91$  and no momentum source and found two regimes of solution. For weak ambient flows

( $\mathcal{U}_p \lesssim 0.37$ ), the current is symmetric close to the source and the particle volume fraction and deposit decay exponentially. For strong ambient flows,  $0.37 \lesssim \mathcal{U}_p \lesssim 1.20$ , the current initially propagates upstream but eventually retreats. For both homogeneous and particle-driven currents, we obtain good agreement between our results and the experimental data of HHH.

Finally we briefly discuss some limits of validity of the shallow-water model using a scaling argument. The total buoyancy force of the current scales as  $\rho_c g' H^2$ , the total inertial force as  $\rho_c V^2 H$ , the total viscous force as  $\nu \rho_c \Delta V L / H$  and the total interfacial drag as  $\rho_c C_D (\Delta V)^2$ . Here  $V$  is a velocity scale for the current,  $H \sim Q / V$  and  $L \sim V \hat{t}$  are vertical and horizontal scales respectively,  $\nu$  is the kinematic viscosity,  $C_D$  is the drag coefficient and  $\Delta V \sim (g' H)^{1/2}$  is the velocity difference between the current and the ambient. On the upstream side of the source, either the force of the ambient flow balances the buoyancy of the current (in which case the flow becomes increasingly like a density wedge: close to the lower boundary the flow is towards the front but at the interface it is away) or  $V \sim (g' H)^{1/2}$  (which reproduces the scalings for a basal-friction-dominated current (Huppert 1982; Hogg & Woods 2001)) or  $V \sim \Delta V \sim (g' H)^{1/2}$ . On the downstream side of the source, either  $V \sim U$  (in which case drag is negligible) or  $V \sim (g' H)^{1/2}$  or  $V \sim \Delta V \sim (g' H)^{1/2}$ . Considering  $V \sim \Delta V \sim (g' H)^{1/2}$ , we find the times to transition to a drag-dominated or viscous-dominated regime are  $\hat{t} \sim Q / C_D U^2$  (HHH) and  $\hat{t} \sim Q^2 / \nu U^2$ . Hence for weak sources, strong ambient flows (in particular our critical values to prevent upstream propagation) or small particle settling speeds, the long-time behaviour we have described may not be observed before interfacial drag or viscous forces affect the motion. The transition to a drag-dominated regime was studied by HHH.

A less quantifiable limitation is the neglect of entrainment. Where the relative Richardson number  $g' \hat{h} / (\hat{u} - U)^2$  is less than a critical value of approximately 0.83, entrainment across the interface occurs (Ellison & Turner 1959). This will be particularly prevalent on the thin downstream section of the current and may substantially alter the height profile (although not the buoyancy profile) and the momentum. In addition, the region immediately exterior to a supercritical source entrains rapidly, potentially becoming subcritical. The current also engulfs and entrains material along the front. For non-Boussinesq currents, the progressively decreasing density difference with respect to the ambient should be reflected in a progressive change in the effective frontal Froude number,  $\beta$ . This modification has not been included in our model. Overall we expect the neglect of entrainment to be the most limiting assumption in our model; however at present it is not possible to estimate its effect.

The authors are grateful to Mark Hallworth for supplying the experimental data of HHH, and to Joel C. Miller, Dominic Vella, Julio Gratton and Marius Ungarish for helpful comments on an earlier draft. This research was partially supported by a PhD studentship to A. C. S. from NERC, award NER/S/A/2002/10337. H. E. H. acknowledges a Royal Society Wolfson Merit Award.

## Appendix A. Source conditions

We provide details of the conditions across a general source for a homogeneous current and briefly discuss implications for a particle-laden one.

In the homogeneous similarity solution structures of § 3.1, the height just exterior to the source is constant in time, thus it is reasonable to consider steady solutions within

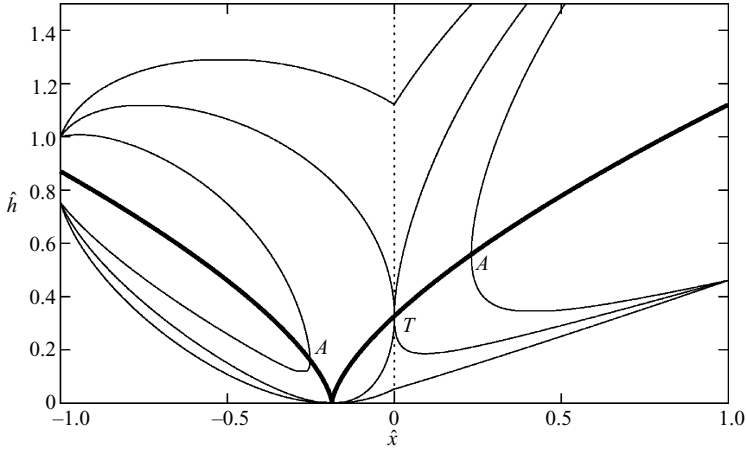


FIGURE 12. Sample (multivalued) height profiles within the source region for the simple source of (2.2) with  $\hat{x}_s = 1$ ,  $Q = 1$ ,  $Q_m = 1$ ,  $g' = 1$ ,  $\hat{h}_{us} = 1$  and  $\hat{u}_{us} = -0.813$ . The inner-most profile has  $Q_d = 1.5$ , the intermediate  $Q_d = 2$  and the outer-most  $Q_d = 2.5$ . The bold curves have  $|\mathcal{F}| = 1$  with  $|\mathcal{F}| < 1$  above and  $|\mathcal{F}| > 1$  below.

the source region. Physically this reflects a balance between advection of material away from the source and supply.

Integrating (2.1 *a, b*) and eliminating  $\hat{u}$  in the resulting expressions, we obtain

$$f(\hat{h}, \hat{x}) \equiv \frac{1}{2}g'\hat{h}^3 - [\hat{u}_{us}^2\hat{h}_{us} + \frac{1}{2}g'\hat{h}_{us}^2 + \mathcal{Q}_m(\hat{x})]\hat{h} + [\hat{u}_{us}\hat{h}_{us} + \mathcal{Q}(\hat{x})]^2 = 0,$$

which needs to be solved for the height,  $\hat{h}$ , at a point  $\hat{x}$  within the source region, where

$$\mathcal{Q}(\hat{x}) = \int_{\hat{x}_{us}}^{\hat{x}} q(\hat{x}') d\hat{x}', \quad \mathcal{Q}_m(\hat{x}) = \int_{\hat{x}_{us}}^{\hat{x}} q_m(\hat{x}') d\hat{x}',$$

$\hat{x}_{us}$  is the maximum upstream extent of the source region and subscript *us* denotes values at that point. Example height profiles for the distribution (2.2) with different  $Q_d$  are shown in figure 12. For general source distributions several features of the corresponding profiles are significant. First, the solutions of  $f = 0$  form two branches for  $g'\hat{h} > 0$ , which merge into one and stop existing where  $d\hat{h}/d\hat{x}$  becomes infinite, or equivalently where the Froude number,  $\mathcal{F} = \hat{u}/(g'\hat{h})^{1/2}$ , has magnitude unity. Examples of such points are labelled *A* in figure 12. Secondly, a steady shock cannot satisfy the Lax entropy condition (2.4), hence a solution cannot transition between the two branches except at a point where  $|\mathcal{F}| = 1$ , as exemplified by point *T* in figure 12. Finally, to ensure flow outward from the source,  $\hat{u}_{us} < 0$  and  $\hat{u}_{ds} > 0$ , where subscript *ds* denotes values at the maximum downstream extent of the source region. Continuity then implies that  $\hat{u} = 0$  at some point within the source region. On the lower branch  $\hat{h} = 0$  at this point.

Thus there are three possible combinations for the flow on either side of the source.

(a) It can be subcritical on both sides.

(b) It can be subcritical on one side and supercritical on the other, which is only possible if there exists a point,  $\hat{x}_s$ , where  $|\mathcal{F}| = 1$  and  $f$  has a saddle.

(c) It can be supercritical on both sides, generally only possible following the lower branch through the point  $\hat{x}_0$  where  $\hat{h} = 0$ , the derivative of the height changes sign and  $\hat{u} = 0$ .

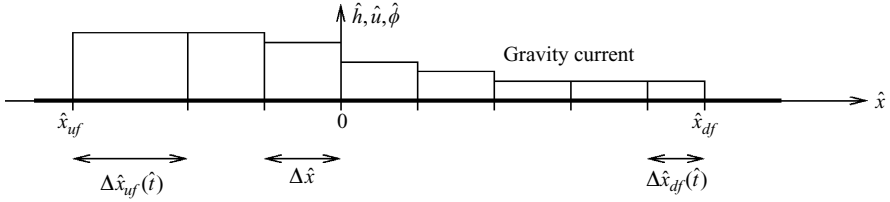


FIGURE 13. The computational domain.

For our simple source (2.2), it may be shown that the transition point  $\hat{x}_t$  and zero point  $\hat{x}_0$  can only occur at the origin, thus (a–c) are equivalent to the combinations given in table 1. For a general source, it may be shown that a point  $\hat{x}_t$  can only exist if

$$\frac{8}{3} g' \frac{q^3}{q_m^2} < \frac{d}{d\hat{x}} \left( \frac{q_m}{q} \right), \quad (\text{A } 1a)$$

at that point, while passing through the point  $\hat{x}_0$  requires

$$q_m(\hat{x}_0) = 0, \quad (\text{A } 1b)$$

provided  $q_m$  is non-zero somewhere within the source region (otherwise  $u_{us}h_{us} = 0$ , a case we need not consider because no fluid propagates upstream). Conditions (A 1) both require the distribution of the momentum source to differ substantially from a constant multiple of the distribution of the volume source, in other words the source must have a finite-momentum dipole. In consequence, if there is only a small-momentum dipole, then  $|\mathcal{F}| < 1$  on both sides of the source, only the total volume and momentum added are important (as described in §3.1) and the details of the source distribution are immaterial.

The same approach may also be applied to particle-laden currents. In particular, if  $\hat{x}_s \ll Q/W_p$ , then  $\hat{\phi}$  remains effectively constant over the source region and equal to  $\phi_0$ . In this case the above results may be used directly.

## Appendix B. Numerical method

Two features of the governing equations (2.1) and boundary conditions (2.6) and (2.7) cause numerical difficulties. First, the equations are nonlinear and hyperbolic, hence shocks may develop despite smooth initial conditions (Kevorkian 1991). Secondly, the boundary conditions apply at a moving front. We employ a finite-volume method to capture any shocks and a front-tracking method to impose the conditions at the moving front. Complete details of the implementation are provided by Slim (2006); here we provide a summary.

The interior of the current is broken up into uniform cells of width  $\Delta\hat{x}$ . At the fronts, the cell sizes  $\Delta\hat{x}_{uf}$  and  $\Delta\hat{x}_{df}$  depend on time and satisfy  $\alpha\Delta\hat{x} \leq \Delta\hat{x}_{uf,df}(\hat{t}) < (1+\alpha)\Delta\hat{x}$  ( $\alpha=0.7$  for the results presented). The computational domain is shown in figure 13. The time-step  $\Delta\hat{t}$  is chosen to satisfy the CFL condition  $v = \max_i |S_i| \Delta\hat{t} / \Delta\hat{x}_i < 1$ , where  $v$  is the imposed CFL number ( $v=1/2$  for the results presented) and  $|S_i|$  is the maximum speed of waves in computational cell  $i$ . We approximate  $|S_i|$  by the speed of rarefactions, although this can overestimate the allowed  $\Delta\hat{t}$  (Toro 1992, 2001) and hence we check the true value of the CFL number at each step.

System (2.1) is decomposed into source terms

$$\frac{d\hat{h}}{d\hat{t}} = q(\hat{x}), \quad \frac{d(\hat{u}\hat{h})}{d\hat{t}} = q_m(\hat{x}), \quad \frac{d(\hat{\phi}\hat{h})}{d\hat{t}} = -W_p\hat{\phi} + \phi_0q(\hat{x}), \quad (\text{B } 1)$$

and hyperbolic terms

$$\frac{\partial\hat{h}}{\partial\hat{t}} + \frac{\partial(\hat{u}\hat{h})}{\partial\hat{x}} = 0, \quad \frac{\partial(\hat{u}\hat{h})}{\partial\hat{t}} + \frac{\partial}{\partial\hat{x}}(\hat{u}^2\hat{h} + \frac{1}{2}g'\hat{h}^2) = 0, \quad \frac{\partial(\hat{\phi}\hat{h})}{\partial\hat{t}} + \frac{\partial(\hat{u}\hat{\phi}\hat{h})}{\partial\hat{x}} = 0, \quad (\text{B } 2)$$

and we use Strang splitting (LeVeque 2002) to alternate between solving (B 1) exactly and (B 2) and the boundary conditions approximately. For homogeneous and particle-laden currents, the hyperbolic terms (B 2) are solved using the (second-order) weighted average flux (WAF) finite-volume method (Toro 1992, 2001) with exact Riemann solvers (Slim 2006). A superbee-like limiter (Toro 1992, 2001) is used to dampen spurious oscillations. For particle-driven currents, we use Godunov's method (LeVeque 2002) because WAF produces slight undershoots on the lower side of shocks, which results in negative heights at the large shocks that develop at long times. For all three types of current we also calculate the flux of momentum through the fronts using Godunov's method and an exact Riemann solver incorporating (2.6) and (2.7). The fronts are evolved according to (2.7) with the frontal velocities provided by the exact solver. This treatment of the boundary conditions is a simple first-order variant of the front tracking method of LeVeque & Shyue (1996).

Detailed validation of the code against analytic solutions for frontal Riemann problem test cases (for which order-one convergence is obtained) and against previous code is presented by Slim (2006). We note that the numerical solutions plotted in § 4 are essentially indistinguishable on reducing the spatial step size.

## REFERENCES

- BENJAMIN, T. B. 1968 Gravity currents and related phenomena. *J. Fluid Mech.* **31**, 209–248.
- BONNECAZE, R. T., HALLWORTH, M. A., HUPPERT, H. E. & LISTER, J. R. 1995 Axisymmetric particle-driven gravity currents. *J. Fluid Mech.* **294**, 93–121.
- BONNECAZE, R. T., HUPPERT, H. E. & LISTER, J. R. 1993 Particle-driven gravity currents. *J. Fluid Mech.* **250**, 339–369.
- CARBONE, R. E. 1982 A severe frontal rainband. Part I: stormwide hydrodynamic structure. *J. Atmos. Sci.* **39**, 258–279.
- CEDERWALL, K. 1971 Buoyant slot jets into stagnant or flowing environments. *Tech. Rep.* KH-R-25. W. M. Keck Lab. of Hydraulics and Water Resources, California Inst. Tech.
- ELLISON, T. H. & TURNER, J. S. 1959 Turbulent entrainment in stratified flows. *J. Fluid Mech.* **6**, 423–448.
- FANNELOP, T. K. & WALDMAN, G. D. 1972 Dynamics of oil slicks. *AIAA J.* **10**, 506–510.
- GRATTON, J. & VIGO, C. 1994 Self-similar gravity currents with variable inflow revisited: plane currents. *J. Fluid Mech.* **258**, 77–104.
- GRÖBELBAUER, H. P., FANNELØP, T. K. & BRITTER, R. E. 1993 The propagation of intrusion fronts of high-density ratios. *J. Fluid Mech.* **250**, 669–687.
- HACKER, J., LINDEN, P. F. & DALZIEL, S. B. 1996 Mixing in lock-release gravity currents. *Dyn. Atmos. Oceans* **24**, 183–195.
- HALLWORTH, M. A., HOGG, A. J. & HUPPERT, H. E. 1998 Effects of external flow on compositional and particle gravity currents. *J. Fluid Mech.* **359**, 109–142.
- HALLWORTH, M. A., HUPPERT, H. E., PHILLIPS, J. C. & SPARKS, R. S. J. 1996 Entrainment into two-dimensional and axisymmetric turbulent gravity currents. *J. Fluid Mech.* **308**, 289–311.
- HARRIS, T. C., HOGG, A. J. & HUPPERT, H. E. 2001 A mathematical framework for the analysis of particle-driven gravity currents. *Proc. R. Soc. Lond. A* **457**, 1241–1272.

- HOGG, A. J., HALLWORTH, M. A. & HUPPERT, H. E. 2005 On gravity currents driven by constant fluxes of saline and particle-laden fluid in the presence of a uniform flow. *J. Fluid Mech.* **539**, 349–385 (referred to herein as HHH).
- HOGG, A. J. & WOODS, A. W. 2001 The transition from inertia- to bottom-drag-dominated motion of turbulent gravity currents. *J. Fluid Mech.* **449**, 201–224.
- HOULT, D. P. 1972 Oil spreading on the sea. *Annu. Rev. Fluid Mech.* **4**, 341–368.
- HOULT, D. P., FAY, J. A. & FORNEY, L. J. 1969 A theory of plume rise compared with field observations. *J. Air Poll. Contr. Assoc.* **19** (8), 585–590.
- HUPPERT, H. E. 1982 The propagation of two-dimensional and axisymmetric viscous gravity currents over a rigid horizontal surface. *J. Fluid Mech.* **121**, 43–58.
- VON KÁRMÁN, T. 1940 The engineer grapples with nonlinear problems. *Bull. Am. Math. Soc.* **46**, 615–683.
- KEVORKIAN, J. 1991 *Partial Differential Equations: Analytical Solution Techniques*. Springer.
- KLEMP, J. B., ROTUNNO, R. & SKAMAROCK, W. C. 1994 On the dynamics of gravity currents in a channel. *J. Fluid Mech.* **269**, 169–198.
- LAX, P. D. 1957 Hyperbolic systems of conservation laws II. *Commun. Pure Appl. Maths* **X**, 537–566.
- LEVEQUE, R. J. 2002 *Finite Volume Methods for Hyperbolic Problems*. Cambridge University Press.
- LEVEQUE, R. J. & SHYUE, K.-M. 1996 Two-dimensional front tracking based on high resolution wave propagation methods. *J. Comput. Phys.* **123**, 354–368.
- LIU, C. H. & MONCRIEFF, M. W. 1996 A numerical study of the effects of ambient flow and shear on density currents. *Mon. Weath. Rev.* **124**, 2282–2303.
- MILLER, J. C. & BERNOFF, A. J. 2003 Rates of convergence to self-similar solutions of Burgers' equation. *Stud. Appl. Maths* **111**, 29–40.
- PEDLOSKY, J. 1987 *Geophysical Fluid Dynamics*, 2nd edn. Springer.
- ROSS, A. N. 2000 Gravity currents on slopes. PhD thesis, University of Cambridge.
- ROTTMAN, J. W. & SIMPSON, J. E. 1983 Gravity currents produced by instantaneous release of a heavy fluid in a rectangular channel. *J. Fluid Mech.* **135**, 95–110.
- SIMPSON, J. E. 1997 *Gravity Currents: In the Environment and the Laboratory*, 2nd edn. Cambridge University Press.
- SIMPSON, J. E. & BRITTER, R. E. 1980 A laboratory model of an atmospheric mesofront. *Q. J. R. Met. Soc.* **106**, 485–500.
- SLIM, A. C. 2006 High Reynolds number gravity currents. PhD thesis, University of Cambridge.
- THORPE, A. J., MILLER, M. J. & MONCRIEFF, M. W. 1980 Dynamical models of two-dimensional downdraughts. *Q.J.R. Met. Soc.* **106**, 463–484.
- TORO, E. F. 1992 Riemann problems and the WAF method for solving the two-dimensional shallow-water equations. *Phil. Trans. R. Soc. Lond. A* **338**, 43–68.
- TORO, E. F. 2001 *Shock-capturing Methods for Free-surface Shallow Flows*. Wiley.
- UNGARISH, M. 2007 A shallow-water model for high-Reynolds-number gravity currents for a wide range of density differences and fractional depths. *J. Fluid Mech.* **579**, 373–382.
- UNGARISH, M. & HUPPERT, H. E. 1998 The effects of rotation on axisymmetric gravity currents. *J. Fluid Mech.* **362**, 17–51.
- VALENTINE, D. T. & KAO, T. W. 1984 Gravity current upstream of a buoyant influx in an open-channel flow – a numerical study. *J. Fluid Mech.* **140**, 303–327.
- WHITHAM, G. B. 1974 *Linear and Nonlinear Waves*. Wiley.